Aerodynamic Design Optimization on Unstructured Meshes Using the Navier-Stokes Equations

Eric J. Nielsen[*]

Virginia Polytechnic Institute and State University, Blacksburg, VA 24060

W. Kyle Anderson[†]

NASA Langley Research Center, Hampton, VA 23681-2199

Abstract

A discrete adjoint method is developed and demonstrated for aerodynamic design optimization on unstructured grids. The governing equations are the three-dimensional Reynolds-averaged Navier-Stokes equations coupled with a one-equation turbulence model. A discussion of the numerical implementation of the flow and adjoint equations is presented. Both compressible and incompressible solvers are differentiated and the accuracy of the sensitivity derivatives is verified by comparing with gradients obtained using finite differences. Several simplifying approximations to the complete linearization of the residual are also presented, and the resulting accuracy of the derivatives is examined. Demonstration optimizations for both compressible and incompressible flows are given.

Introduction

As computational power has continued to advance in recent years, researchers have been able to extend the use of computational tools to increasingly more complex problems. Computational fluid dynamics (CFD) has been exploited as an analysis tool for some time, and is currently receiving attention as a design optimization tool. Early attempts in CFD-based design problems made use of finite-difference calculations to obtain sensitivity information. This technique can be used to obtain the derivatives of all the flow quantities with respect to each design variable and can be easily retrofitted to existing flow solvers. One problem with this approach is the computational time required. To obtain the design sensitivities for a system involving n design parameters using a central-difference approach requires well-converged solutions of $2n$ flow analysis problems. For complex cases with many design variables, this requirement may become prohibitive. Another problem often encountered with the finite-difference approach is the sensitivity of the derivatives to the choice of the step size. It is desirable to have a small step size so that the truncation error is minimal, while at the same time, avoid exceedingly small step sizes which could yield large cancellation errors.

To mitigate the difficulties associated with the choice of step size used in finite differences, direct differentiation can be employed.[14, 19, 25] In this approach, the sensitivity derivatives of all the variables in the flow field are obtained but the solution of a large linear system of equations for each design variable is required. Therefore, for problems involving many design variables, obtaining the sensitivity derivatives can be expensive.

In recent years, adjoint formulations have grown in popularity, and are rapidly being developed for use in aerodynamic design sensitivity computations (see e.g. Refs. 2, 4, 9, 10, 15, 18). The adjoint approach has the advantage of being able to compute cost function gradients at an expense independent of the number of design parameters. This feature makes adjoint methods extremely attractive for problems involving a large number of design variables.

In the current work, a discrete adjoint approach is used in an unstructured-grid framework to compute design sensitivities for problems based on the Navier-Stokes equations. A one-equation turbulence model is used which is fully differentiated and coupled into the solution of the adjoint equations so that the resulting sensitivity derivatives are consistent with those obtained using finite differences. In addition to a compressible solver, an incompressible formulation is also differentiated in order to accommodate a wide range of applications. The accuracy of the resulting derivatives is established and sample calculations are shown for two- and three-dimensional cases using both implementations. Conclusions and suggestions for future research are also given.

Nomenclature

a	Speed of sound
C^*	Sutherland's constant
C_l, C_d	Lift and drag coefficients
C_l^*, C_d^*	Target lift and drag coefficients
$\overline{C}_{l_{trans}}$	Ratio of lift derivatives for translation
$c_{b_1}, c_{b_2}, c_{v_1}$	Constants for turbulence model
$c_{w_1}, c_{w_2}, c_{w_3}$	Constants for turbulence model
D	Vector of design variables
d	Distance to the nearest surface
E	Total energy per unit volume
$\hat{F}_i$	Inviscid flux vector
$\hat{F}_v$	Viscous flux vector
f	Cost function
f_v, g_v, h_v	Components of viscous fluxes
f_{v_1}, f_{v_2}	Functions for turbulence model
f_w, f_{t_1}, f_{t_2}	Functions for turbulence model
g	Function for turbulence model
I	Identity matrix
$\hat{i}, \hat{j}, \hat{k}$	Unit vectors in Cartesian coordinate directions
K_{ij}	Spring constant for mesh movement
L	Lagrangian function
l	Length of face

[*]Graduate Student, Aerospace and Ocean Engineering Department, Student Member AIAA.
[†]Senior Research Scientist, Aerodynamic and Acoustic Methods Branch, Fluid Mechanics and Acoustics Division, Assoc. Fellow, AIAA.

M	Mach number
$\hat{n}$	Outward-pointing normal to control volume
Pr	Prandtl number
Pr_t	Turbulent Prandtl number
p	Pressure
Q	Vector of conserved variables
q_x, q_y, q_z	Components of heat flux
R	Residual for a control volume
Re	Reynolds number
r	Function for turbulence model
S	Magnitude of vorticity
T	Temperature
t	Time
u, v, w	Cartesian components of velocity
V	Volume of control volume
X	Grid-point locations
x, y, z	Cartesian coordinate directions

Greek

α	Angle of attack
γ	Ratio of specific heats
Ω	Boundary of control volume
κ	Constant for turbulence model
Λ	Vector of Lagrange multipliers
μ	Laminar viscosity
μ_t	Turbulent viscosity
υ	μ/ρ
υ_t	μ_t/ρ
$\tilde{\upsilon}$	Dependent variable for turbulence model
ρ	Density
σ	Constant for turbulence model
τ_{ij}	Components of shear stress
χ	Function for turbulence model
ω_1, ω_2	Weights for lift and drag in cost function

Subscripts

∞	Free-stream quantity

Governing Equations

The governing equations are the three-dimensional Reynolds-averaged Navier-Stokes equations. In the present work, both the compressible and incompressible forms of these equations are considered. For turbulent flows, the one-equation turbulence model of Spalart and Allmaras[27] is used. The compressible flow equations, as well as the equations for the turbulence model, are given in Appendix A.

Adjoint and Design Equations

In the adjoint approach for design optimization, a cost function is defined and augmented with the flow equations as constraints to form a Lagrangian given by

$$L(D, Q, X, \Lambda) = f(D, Q, X) + \Lambda^T R(D, Q, X) \qquad (1)$$

Here, $f(D, Q, X)$ is the cost function to be minimized and D is a vector of design variables. The vector of Lagrange multipliers (also known as costate variables) is denoted by Λ, and R is the residual of the discretized steady-state flow equations. The vector Q is the conserved variables and X represents the computational grid. Although not explicitly denoted in Eq. 1, both Q and X are functions of the design variables.

Differentiating Eq. 1 with respect to the design variables yields

$$\frac{dL}{dD} = \left\{ \frac{\partial f}{\partial D} + \left[\frac{\partial X}{\partial D} \right]^T \frac{\partial f}{\partial X} \right\} + \qquad (2)$$

$$\left[\frac{\partial Q}{\partial D} \right]^T \left\{ \frac{\partial f}{\partial Q} + \left[\frac{\partial R}{\partial Q} \right]^T \Lambda \right\} + \left\{ \left[\frac{\partial R}{\partial D} \right]^T + \left[\frac{\partial X}{\partial D} \right]^T \left[\frac{\partial R}{\partial X} \right]^T \right\} \Lambda$$

Because Λ is arbitrary, the terms multiplied by $\left[\frac{\partial Q}{\partial D} \right]^T$ may be eliminated using the following equation

$$\left[\frac{\partial R}{\partial Q} \right]^T \Lambda = -\left(\frac{\partial f}{\partial Q} \right) \qquad (3)$$

Equation 3 is a linear system which represents the discrete adjoint equation for the optimization problem. After the flow equations have been solved for Q, the adjoint equation can be solved for the unknown vector of Lagrange multipliers Λ. The remaining terms in Eq. 2 can be used to evaluate the sensitivity derivatives as follows:

$$\frac{\partial L}{\partial D} = \left\{ \frac{\partial f}{\partial D} + \left[\frac{\partial X}{\partial D} \right]^T \frac{\partial f}{\partial X} \right\} + \left\{ \left[\frac{\partial R}{\partial D} \right]^T + \left[\frac{\partial X}{\partial D} \right]^T \left[\frac{\partial R}{\partial X} \right]^T \right\} \Lambda \qquad (4)$$

After the solution for the costate variables is obtained using Eq. 3, the vector containing all of the desired sensitivities can be evaluated as a single matrix-vector product, given by Eq. 4.

Numerical Implementation

Flow Equations

The flow solvers used in the current work are described at length in Refs. 1, 3, and 5. The codes use an implicit, upwind, finite-volume discretization, in which the dependent variables are stored at the mesh vertices. Inviscid fluxes at cell interfaces are computed using the upwind schemes of Roe,[21] van Leer,[29] or Osher.[6] Viscous fluxes are formed using an approach equivalent to a central-difference Galerkin procedure. Temporal discretization is performed using a backward-Euler time-stepping scheme, and multigrid acceleration can be used for the two-dimensional codes.[5]

An approximate solution of the linear system of equations formed at each time step is obtained using several iterations of a point-iterative scheme in which the nodes are updated in an even-odd fashion, resulting in a Gauss-Seidel-type method.

The turbulence model is solved separately from the flow equations at each time step, using a backward-Euler time-stepping scheme. The resulting linear system is solved using the same point-iterative scheme employed for the flow equations. The turbulence model is integrated all the way to the wall without the use of wall functions.

The incompressible solvers are based on an artificial compressibility formulation, and are described in Ref. 3. Time integration and solution of the linear system at each time step are performed in the same manner as described above.

Adjoint and Design Equations

The adjoint equation given in Eq. 3 represents a linear set of equations for the costate variables Λ. Although this system can be solved directly using GMRES,[22] a time-like derivative is added and the solution is obtained by marching in time, much like the flow solver:

$$\left\{ \frac{V}{\Delta t} I + \left[\frac{\partial R}{\partial Q} \right]^T \right\} \Delta^n \Lambda = -\frac{\partial f}{\partial Q} - \left[\frac{\partial R}{\partial Q} \right]^T \Lambda^n \tag{5}$$

where

$$\Lambda^{n+1} = \Lambda^n + \Delta^n \Lambda \tag{6}$$

The time term can be used to increase the diagonal dominance for cases in which GMRES alone would tend to stall. This ultimately results in a more robust adjoint solver.

Due to the large amount of code resulting from the linearization of the viscous terms and the turbulence model, these contributions are stored in the present implementation. Because the stencil for the inviscid contributions is larger, the linearization of these terms is recomputed at each step to avoid the need for extra storage and data structure.

To precondition the linear system, an incomplete LU decomposition of the matrix obtained from a first-order accurate discretization is used. The preconditioning is applied on the left and no fill-in is allowed (ILU[0]).[13] Numerical experiments using this preconditioner have shown that some turbulent cases are slow to converge. An alternate means of preconditioning that has often been found useful is to employ a point-iterative scheme similar to that used for the flow equations. This technique allows for continual improvement in preconditioning the first-order system but is most effective when the time step is small and the matrix is diagonally dominant.

In the present work, the differentiation of both the flow equations and the turbulence model is accomplished by "hand differentiating" the code. For obtaining the solution of the adjoint equations, the turbulence model is tightly coupled during the solution process, whereas it is solved separately during the flow analysis. During development, various treatments of the turbulence model have been studied and it has been found that the close coupling of the turbulence model is required in order to obtain sensitivity derivatives consistent with those obtained using finite differences. This will be illustrated in a subsequent section.

Cost Functions

For both two and three dimensions, the cost function is composed of a linear combination of the lift and drag coefficients:

$$f = \omega_1 (C_l - C_l^*)^2 + \omega_2 (C_d - C_d^*)^2 \tag{7}$$

For two-dimensional calculations, a target pressure distribution can also be specified.

The drag can be minimized while maintaining a specified lift by adjusting the weights associated with each term in Eq. 7. The weights must be chosen such that neither term dominates the other. The current method for choosing the initial weights is to simply set the ratio of ω_2 to ω_1 to be equal to the ratio of the lift to the drag:

$$\frac{\omega_2}{\omega_1} = \frac{C_l}{C_d} \tag{8}$$

During the design process, these weights may require adjustment. However, this avoids the need to solve separate adjoint equations for lift and drag.

Design Variables

For both incompressible and compressible flows, the angle of attack can be utilized as a design variable in addition to the shape. For compressible flows, the free-stream Mach number can also be specified as a design parameter. When the shape is evolving, the surfaces are parameterized as described in the following sections.

Two-Dimensional Parameterization

For two-dimensional cases, the geometry is described using B-splines and the coordinates of the control points are used as design variables as described in Refs. 2 and 4. Translation and rotation of individual bodies can also be used as design variables. Although not discussed further here, a graphical interface has been developed which aids the user in selecting and placing limits on design variables, as well as modifying target pressure distributions.[2] This interface has proven to be very useful and helps reduce errors in setting up design cases.

Three-Dimensional Parameterization

The three-dimensional code has been coupled with a geometric parameterization scheme recently introduced by Samareh.[23] The method utilizes a free-form deformation technique similar to that used in the motion picture industry for animating digital images. Here, a Bezier net describing the changes in the geometry is placed around the baseline mesh. The control points in the net may be used directly as the design variables, or they may be further grouped into design variables such as camber, thickness, and twist. This parameterization technique has been chosen for its ability to handle arbitrary geometries and because the mesh generation process does not depend on a prior parameterization of the geometry. This allows meshes which have been previously generated solely for analysis to be utilized for design purposes.

Geometric Constraints

During the design process, the feasibility of the geometry is maintained by limiting the movement of the design variables. For the two-dimensional code, area and curvature constraints may also be placed on the geometry although these are not employed in the present work. The curvature constraints can be used to enforce a specified leading edge radius or to guarantee curvatures of a specified sign.

Grid Generation and Mesh Movement Strategy

For all of the two-dimensional computations, the meshes have been generated using the method described in Ref. 17. In three dimensions, the method of Ref. 20 is utilized. Both techniques employ an advancing front methodology and generate good quality grids for both inviscid and viscous calculations.

When the design process requires modifications to the surface geometry, the computational mesh must be deformed to reflect the changes. For inviscid flows, the mesh movement strategy is based on the spring analogy described in Ref. 30. The edges of the mesh are treated as tension-springs, and the following equation is solved using a Jacobi iteration process:

$$\sum_{j \in N_i} K_{ij} (\Delta x_i - \Delta x_j) = 0 \tag{9}$$

Here Δx_i and Δx_j represent the change in the coordinates of nodes i and j from the initial mesh to the desired mesh. The spring constants K_{ij} are assumed to be l_{ij}^{-2}, where l is the length of the edge connecting node i to node j. Since this technique may result in crossed grid lines, the required shift of the surface coordinates is decomposed into a series of smaller movements (usually around 10), and Eq. 9 is relaxed for each change in the surface. This strategy has been found to work well for Euler-based designs.

For viscous meshes, the method described above is not adequate and can easily lead to crossing mesh lines and negative volumes. For these cases, the nodes near viscous surfaces are shifted by interpolating the changes in the coordinates at the boundaries of the nearest surface triangle or edge. This technique is blended with a smoothing procedure so that away from the highly stretched cells near the surface, the mesh movement reverts to that of the procedure described above for inviscid meshes. Further details can be found in Ref. 4.

For two-dimensional viscous applications, the procedure described above is very robust and is capable of successfully deforming the mesh in response to large changes in the surface geometry. For multielement airfoils, there is a tendency to open "gaps" in the mesh between elements when the elements are allowed to translate away from one another. A similar problem occurs when the elements move closer together in which case there is a "jamming" together of mesh points. These difficulties are simply due to the fact that no additional mesh points are inserted or removed during the process so that as elements shift in relation to one another, voids can be created. This has not had a detrimental effect on the flow solver and can be remedied by periodically regenerating the mesh.

For three-dimensional flows, the mesh movement procedure is inadequate when large changes in the geometry are required. In these cases, negative cell volumes can occur around the edges of the planform. Therefore, changes in the thickness and camber have been limited to only a few percent of the chord. Further research is required to develop a more reliable methodology for large geometric changes in three dimensions.

As the surface is deformed during the design process, there is a corresponding change in the interior mesh points as well. The effect of the changing grid is reflected through the mesh sensitivity terms given by $\partial X/\partial D$ in Eq. 4. The computation of these terms is achieved by differentiating the mesh movement process described above.

Optimization Technique

The optimization technique used in all of the results presented below is the quasi-Newton method of Davidon-Fletcher-Powell.[8,11] The current implementation of this technique, referred to as KSOPT, allows for multipoint optimization as well as both equality and inequality constraints.[32] For the present work, the multipoint capability is not utilized although this is an obvious future requirement.

Results and Discussion

Consistency of Linearization

During code development, great care has been taken at each step to ensure that the derivatives are consistent with those obtained using finite differences. In this section, the accuracy of the resulting derivatives is verified for compressible flow in both two and three dimensions. Similar results have been obtained for incompressible flows and are included in Appendix B. Comparisons are made between derivatives computed using finite differences with those obtained using the adjoint method. When computing derivatives using finite differences, central-difference formulas are used with a step size of 1×10^{-5}, and the flow solver is converged to machine accuracy. The two-dimensional results shown are calculated using the Osher flux function although similar accuracy is obtained using either flux-difference splitting or flux-vector splitting. For the three-dimensional linearizations, all results are obtained using the flux-difference splitting scheme of Roe. All of the results shown below are for turbulent flows although the consistency of derivatives has been verified for inviscid and laminar flows as well.

Two-Dimensional Accuracy

For demonstrating the consistency of the derivatives obtained using the adjoint formulation with those obtained using finite differences, two test cases are considered. The first case is a 2-element airfoil at a free-stream Mach number of 0.25, an angle of attack of $1°$, and a Reynolds number of 9 million based on the chord of the airfoil. The geometry has been chosen arbitrarily and is that given in Ref. 31.

The mesh used for this test has 4,901 nodes and is shown in Fig. 1. The geometry of each airfoil is described with a third-order B-spline. The derivatives of the lift and drag coefficients with respect to the vertical and horizontal positions of four shape design variables have been obtained. The locations of the design variables are indicated by the solid circles shown in Fig. 2. As seen in the fig-

ure, two of these design variables are located on the main airfoil and two are located on the flap. For each element, one design variable is located on the upper surface near the nose of the airfoil and one is located near the rear. A comparison of derivatives of the lift and drag coefficients with respect to changes in the vertical position of these design variables is shown in Tables 1 and 2, while Tables 3 and 4 compare the derivatives of the lift and drag coefficient with respect to x- and y-translation of the flap. Note that this required two solutions of the adjoint equation — one for lift and one for drag. As seen, the derivatives obtained with the adjoint approach are in very good agreement with the finite-difference derivatives for all cases. Although not shown, similar accuracy is obtained for the derivatives with respect to horizontal changes in the control points.
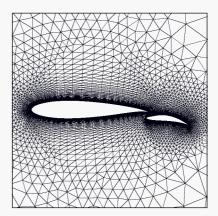

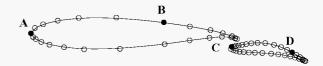**Figure 1. Mesh for 2-element airfoil used in assessment of two-dimensional design sensitivities.**

Figure 2. Location of design variables for 2-element airfoil.

Table 1. Accuracy of two-dimensional derivatives for lift coefficient

	Finite difference	Adjoint	% Diff.
M_∞	0.30965	0.30962	-0.010
α	0.12285	0.12282	-0.024
Point A	-1.0952	-1.0952	0.000
Point B	0.57480	0.57480	0.000
Point C	-2.1368	-2.1366	-0.009
Point D	0.76215	0.76215	0.000

In order to further demonstrate the accuracy of the differentiation, a case containing transonic flow is examined. An RAE 2822 airfoil is used at an angle of attack of $2.81°$, a Mach number of 0.75, and a Reynolds number of 6.2 million. The mesh contains 14,127 nodes and the spacing at the wall is 1×10^{-5}. The computed pressure distribution is shown in Fig. 3 along with the corresponding experimental data.[7] For this case, a strong shock is present on the upper surface which separates the flow immediately downstream. The locations of the three design variables are shown by the filled circles in Fig. 4. The corresponding sensitivity derivatives for the lift coefficient with respect to a vertical movement of the con-

Table 2. Accuracy of two-dimensional derivatives for drag coefficient

	Finite difference	Adjoint	% Diff.
M_∞	-0.05029	-0.05029	0.000
α	0.00843	0.00843	0.000
Point A	0.21925	0.21925	0.000
Point B	-0.03489	-0.03489	0.000
Point C	0.17007	0.17007	0.000
Point D	0.06447	0.06448	0.016

Table 3. Accuracy of two-dimensional derivatives of lift coefficient for flap translation

	Finite difference	Adjoint	% Diff.
x-translation	1.4226	1.4232	0.042
y-translation	-6.8991	-6.8990	-0.001

Table 4. Accuracy of two-dimensional derivatives of drag coefficient for flap translation

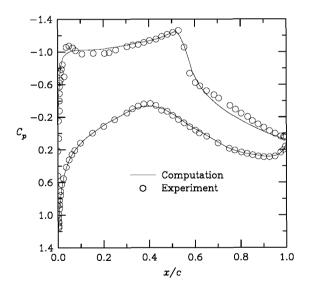|	Finite difference	Adjoint	% Diff.
x-translation	0.02710	0.02716	0.221
y-translation	-0.24164	-0.24163	-0.004

Figure 3. Pressure distribution for transonic RAE 2822 airfoil.

Figure 4. Location of design variables for RAE 2822 airfoil.

trol points are listed in Table 5 along with those for Mach number and angle of attack. The agreement with finite differences is very good, although the derivative for the design variable located in the separated region of the flow just downstream of the shock appears to be slightly inconsistent. However, numerical experiments using different step sizes have shown that finite differences for this control point are somewhat sensitive to the perturbation level. For example, step sizes of 1×10^{-6} and 5×10^{-5} result in finite-difference derivatives of 1.9187 and 1.9150 respectively.

Table 5. Sensitivity derivatives for lift coefficient for RAE 2822 airfoil

	Finite difference	Adjoint	% Diff.
M_∞	-3.0546	-3.0546	0.000
α	5.7614	5.7615	0.002
Point A	7.9826	7.9814	-0.015
Point B	1.9247	1.9219	-0.145
Point C	1.3283	1.3283	0.000

Three-Dimensional Accuracy

To verify the accuracy of the derivatives in three dimensions, a similar experiment is conducted. For this case, an ONERA M6 wing[24] has been parameterized using 46 design variables describing the planform, twist, shear, thickness, and camber. The design variables are depicted in Fig. 5 where twist and wing shear have been parameterized at five spanwise locations. The thickness and camber have also been parameterized using the six locations shown in the figure. The design variables describing the planform are not shown in the figure nor are thickness and camber design variables along the leading and trailing edges. The mesh used for these tests contains 16,391 nodes and 90,892 tetrahedra and is shown in Fig. 6. The flow conditions are an angle of attack of 2°, a Reynolds number of 5 million based on the mean chord, and a Mach number of 0.3. In this test, the cost function is a combination of the lift and drag coefficients so that only one adjoint solution is required. The derivatives of the cost with respect to the angle of attack and the Mach number as well as the derivatives with respect to four of the shape parameterization variables are shown in Table 6. As can be seen, the consistency between the derivatives obtained with the adjoint formulation and finite differences is excellent. Additional derivatives for the design variables depicted in Fig. 5 have also been verified with comparable accuracy.
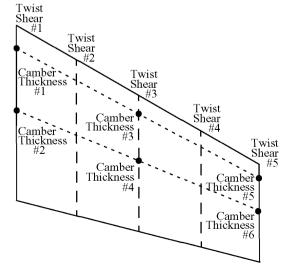

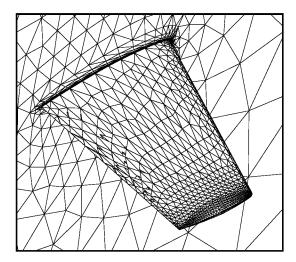**Figure 5. Location of design variables for ONERA M6 wing.**

Figure 6. Grid used for assessment of three-dimensional design sensitivities.

Table 6. Three-dimensional compressible derivatives

	Finite difference	Adjoint	% Diff.
Mach Number	0.00960	0.00959	-0.104
α	-0.03243	-0.03243	0.000
Twist #3	0.00965	0.00965	0.000
Shear #3	-0.04275	-0.04277	0.047
Thickness #3	-0.04011	-0.04012	0.025
Camber #4	-1.3174	-1.3174	0.000

Linearization Approximations

Due to the complexity in achieving accurate linearizations for use in Eqs. 3 and 4, one may consider the use of simplifying assumptions. Clearly, a great deal of effort can be avoided if certain terms may be neglected or replaced with simpler approximations without seriously compromising the accuracy of the results. The previous sections have established the accuracy of the derivatives obtained from the adjoint formulation using a consistent linearization of the flow solvers. This section will examine the accuracy of the derivatives obtained using several natural approximations. These numerical experiments are conducted in two dimensions using the test case and flow conditions used for Table 1. A discussion of each of the approximations is given below and some representative derivatives for vertical changes in the design variables are shown in Table 7.

First-Order Adjoint Solution

For second-order accurate schemes, the complete linearization of the inviscid contribution to the residual requires information from mesh points beyond the immediately adjacent nodes. This requirement arises from having to form gradients of the dependent variables at the nodes in order to extrapolate them to the faces of each control volume. This large stencil makes an exact linearization quite tedious. However, if the fluxes are formed using only nearest-neighbor information, the amount of coding required above the baseline flow solver is minimal. This corresponds to using a first-order accurate scheme for the convective terms, and may also result in a linear system that is easier to solve, as the bandwidth of the coefficient matrix is reduced significantly.

Table 7. Sensitivity derivatives for lift coefficient using various approximations (see Fig. 1)

	Finite difference	Adjoint	% Diff.
Exact Linearization			
Point A	-1.0952	-1.0952	0.000
Point B	0.57480	0.57480	0.000
Point C	-2.1368	-2.1366	-0.009
Point D	0.76215	0.76215	0.000
x-translation (flap)	1.4226	1.4232	0.042
y-translation (flap)	-6.8991	-6.8990	-0.001
First-Order Adjoint			
Point A	-1.0952	0.34633	-132
Point B	0.57480	0.47104	-18.1
Point C	-2.1368	-0.10590	-95.0
Point D	0.76215	0.70373	-7.67
x-translation (flap)	1.4226	-0.68201	-148
y-translation (flap)	-6.8991	0.14801	-102
Constant μ_t			
Point A	-1.0952	-1.6844	53.8
Point B	0.57480	0.37262	-35.2
Point C	-2.1368	-2.2888	7.11
Point D	0.76215	0.57459	-24.6
x-translation (flap)	1.4226	1.1909	-16.3
y-translation (flap)	-6.8991	-7.6163	10.4

In Table 7, derivatives obtained using a first-order linearization of the convective terms are compared with those obtained from the linearization of the higher order residual. For these results, the first-order approximation is made in evaluating both Eqs. 3 and 4. Using this approximation, the derivative of the lift with respect to a vertical shift of the design variable towards the rear of the flap is within 8% of the correct value. However, the derivatives obtained by ignoring the higher order terms are generally highly inaccurate and several are of incorrect sign. The derivatives of incorrect sign would most certainly have an adverse effect on an optimization process, especially near a minimum.

"Frozen" Turbulence Model

An accurate linearization of the turbulence model can be difficult to obtain. As seen from the equations given in Appendix A, there are many terms and additional functions that must be properly differentiated. These terms exhibit complex dependency on both the flow variables as well as the distance to the wall. By assuming that the turbulence model is "frozen", a significant reduction in the required level of effort may be obtained. This approach has been previously used in Refs. 15 and 26 for structured grid applications to airfoils and wings. In these references, successful optimizations have been performed although the accuracy of the derivatives has not been explicitly demonstrated.

Results obtained by making the assumption of a constant eddy viscosity are listed in Table 7. While the computed sensitivities show a large amount of error when compared to finite differences, they all exhibit the correct sign. However, for derivatives associated with horizontal changes in these same design variables, several are of incorrect sign. For example, the finite-difference derivative obtained by perturbing point A in the horizontal direction is -0.18060 whereas the current approximations to the linearizations yield 0.30328. For this same design variable, the complete linearization yields -0.18052 which is less than 0.05 percent in error.

A similar technique that can be used to simplify the implementation is to neglect the contributions from the turbulence model in Eq. 4. This is primarily motivated by the observation that the costate variable associated with the turbulence model is very small

and decays rapidly away from the body. Although not shown, numerical experiments indicate that the resulting accuracy is poor with many derivatives of incorrect sign.

Extent of Mesh Sensitivities

For each design variable, the evaluation of Eq. 4 requires a matrix-vector product of the costate variables with the linearization of the residual. This also includes computation of the mesh sensitivities for each design variable. For large numbers of design variables and mesh points, this can potentially represent a significant expense due to the complicated linearization of the residual. Because nodes further away from the body are subjected to more moderate changes than those in the immediate vicinity of the surface, it may be possible to neglect terms in Eq. 4 that are sufficiently far from the body. This could help to reduce the cost of evaluating Eq. 4 by avoiding the need to include terms from every mesh point in the field.

To investigate the validity of this assumption, a region around the surface of the airfoil is defined by first "tagging" the nodes on the surface and then identifying nodes that lie within a set number of grid layers adjacent to the surface. Outside of this region, the mesh sensitivities are set to zero to emulate the effect of neglecting all the contributions outside of the tagged region. The sensitivity derivatives for the lift coefficient with respect to vertical and horizontal translations of the flap are computed for a varying number of grid layers and the results are shown in Fig. 7. Here, $\bar{C}_{l_{trans}}$ is the ratio of the approximate derivative to the derivative obtained by including the mesh sensitivities at every grid point in the domain. In this figure, the curve labeled n/n_{tot} is the ratio of the number of nodes where mesh sensitivities are employed to the total number of nodes in the mesh. It should be noted that examining a single derivative may not be representative of the behavior of the rest of the derivatives and an accurate computation of this derivative does not guarantee accuracy for the remaining derivatives. However, inaccuracy of this derivative demonstrates that neglecting the full effects of the mesh sensitivities may have an adverse effect on other derivatives as well.

As seen in the figure, the influence of the mesh sensitivities gradually decays away from the surface. Accurate results are obtained when the number of mesh layers is greater than approximately 15. At this point, about half the total number of points in the mesh is included in the layers so that a factor of 2 savings could be realized when evaluating Eq. 4. When many design variables are present, neglecting some of the mesh sensitivities could lead to a substantial savings in computer time. However, for the present study, the computer time required for evaluating Eq. 4 does not dominate the overall optimization process so this strategy is not used.
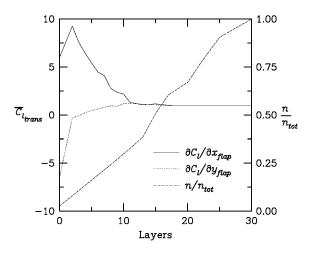

Figure 7. Extent of mesh sensitivity terms required for translation sensitivity accuracy.

Design Examples

Inviscid Multielement Airfoil

The objective of the first example computation is to position the elements on a multielement airfoil to obtain a desired pressure distribution. For this case, the target pressure distribution is obtained from analysis of a baseline configuration.[28] The individual elements are then perturbed by translating in the x- and y-directions as well as by rotating by several degrees. The mesh used for this test contains 3,820 nodes with 193 nodes on the surface of the main element and 129 on each flap. The initial and target configurations are shown in Fig. 8.

The initial pressure distributions over the elements are shown in Fig. 9 along with the target pressure distribution and the pressures obtained after 15 design cycles. A near-field view of the corresponding geometries are shown in Fig. 10. As seen in the figures, the target pressure distributions are obtained and each of the elements returns to its desired position. This experiment has been successfully performed using both the compressible and incompressible solvers, although only results from the incompressible case are shown.
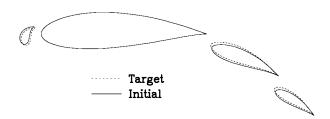

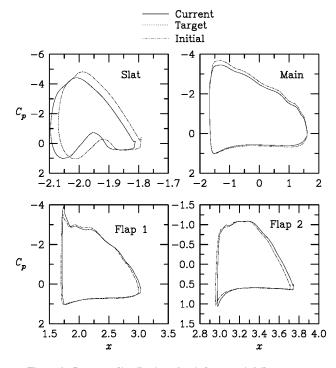**Figure 8. Four-element airfoil in original and perturbed positions.**

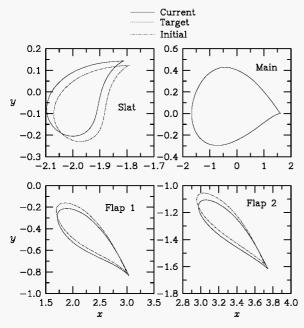**Figure 9. Pressure distributions for 4-element airfoil.**

7

Figure 10. Geometries for 4-element airfoil.

Turbulent Airfoil

The objective for the next test case is to reduce the drag on the RAE 2822 airfoil. The initial flow conditions are a free-stream Mach number of 0.75, an angle of attack of $2.81°$, and a Reynolds number of 6.2 million based on the chord of the airfoil. These conditions correspond to those presented earlier for verifying the shape sensitivity derivatives. For this case, there are 47 active design variables. The lift coefficient is held fixed at 0.7336 and the objective is to reduce the drag coefficient. After 10 design cycles, the drag has been reduced from 0.0263 to 0.0150 whereas after 20 design cycles, a modest improvement is further obtained, reducing the drag coefficient to 0.0149. The initial and final pressure distributions are shown in Fig. 11 and Mach number contours are shown in Fig. 12. As seen in the figures, the shock wave on the surface of the airfoil is eliminated although the curvature in the Mach contours for the final geometry indicate that a shock may form at off-design conditions.

Multielement Airfoil

For this case, the objective is to increase the downforce for a multielement airfoil used for open-wheel racing cars. This airfoil has been initially designed using the inviscid design techniques described in Ref. 12. The mesh has 15,446 nodes with 195 placed on the main element and 129 on the flap. The spacing at the wall is 1×10^{-5} giving a $y^+ \approx 1$ based on flat plate estimates. The Reynolds number is 2.4 million based on the chord of the airfoil and the angle of attack is held fixed at $12°$ which corresponds to the operating point suggested in Ref. 12. After 25 cycles using 65 design variables, the downforce coefficient has increased from -2.3068 to -2.4379. The initial and final pressure distributions computed using the incompressible solver are shown in Fig. 13 along with the corresponding shapes. It is seen from the figure that the redesigned main element carries more downforce compared to the initial design, while the loading on the flap has decreased. Velocity contours and vectors, shown in Fig. 14, indicate that the region of separated flow on the rear of the flap has been reduced through the design process. Although not shown, comparable cases have been run using the compressible code with similar results.
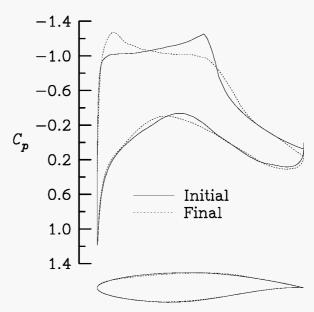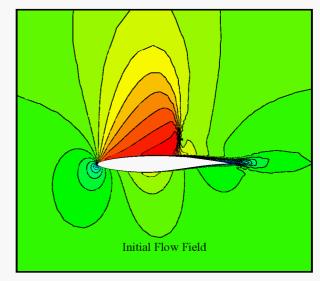

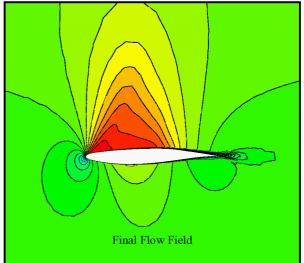Figure 11. Initial and final pressure distributions for drag reduction on RAE 2822 airfoil.

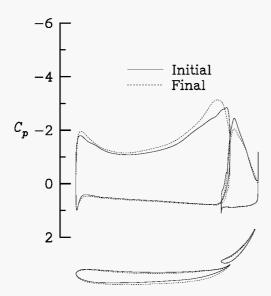Figure 12. Initial and final Mach contours for transonic airfoil optimization exercise.
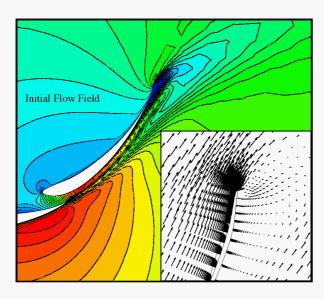
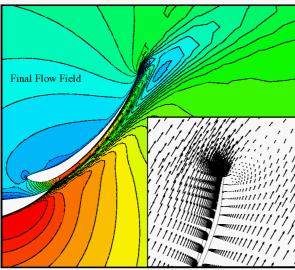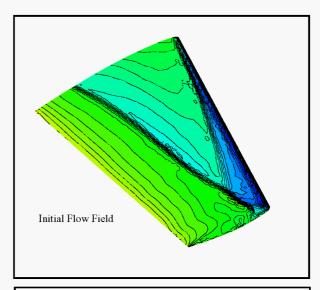**Figure 13. Initial and final pressure distributions for multielement airfoil.**

Figure 14. Velocity contours and vectors in flap region for multielement airfoil.

Inviscid Drag Reduction for ONERA M6 Wing

An example optimization is conducted for inviscid flow over the ONERA M6 wing.[24] The free-stream Mach number for this case is 0.84 and the angle of attack is 3.06°. The mesh used for this computation consists of 53,961 nodes and 287,962 tetrahedrons. The contours for the initial and final density distribution on the surface of the wing are shown in Fig. 15 with the corresponding pressure distributions shown in Fig. 16. The objective of the optimization is to reduce the drag while maintaining a specified lift. For this design, the angle of attack is allowed to change in addition to 10 shape design variables (4 twist, 4 camber, and 2 thickness). The twist variables are located at the 4 outboard stations in Fig. 5 and allowed to increase or decrease by 1°. The thickness and camber variables at positions 3 and 4 are also design variables as is the camber at positions 5 and 6. Each of these is allowed to change by 2 percent of the span. After 10 design cycles, the drag has been reduced from 0.0182 to 0.0167 while the lift has been maintained. The pressure distribution shown in Fig. 16 indicates that the shock has weakened at all of the spanwise stations.
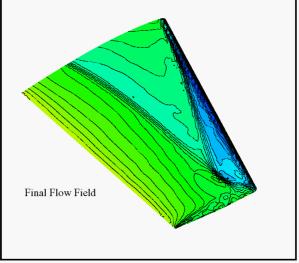

Figure 15. Initial and final density contours for inviscid wing design.
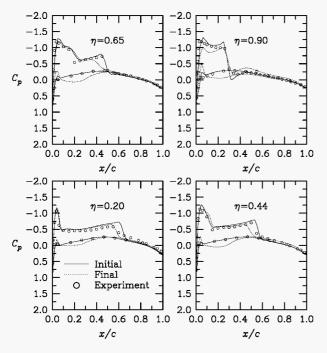
Figure 16. Initial and final pressure distributions for inviscid wing design.
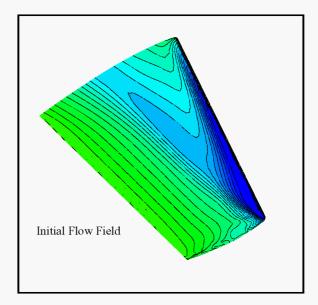
Turbulent ONERA M6 Wing Redesign

A transonic wing design has been conducted using an ONERA M6 mesh consisting of 62,360 nodes and 355,814 tetrahedra. The mesh used for this study is extremely coarse and is not adequate for accurate computations; it serves merely as an initial demonstration for evaluating the methodology. The flow is assumed to be fully turbulent at a Mach number of 0.84, an angle of attack of 3.06°, and a Reynolds number of 5 million. For this flow field, a weak swept shock extends from the root leading edge and a normal shock is present further aft on the wing surface (see Fig. 17). The weakness of the shock is in large part due to the coarseness of the mesh; further refinement would yield a shock structure similar to that shown in the initial flow field in Fig. 15. The objective of the design is to reduce the drag while holding the lift constant. For this case, thickness and camber have been allowed to vary at two chordwise stations located at the mid-span of the wing. These design variables have been allowed to change up to 1 percent of the span of the wing. The angle of attack is also allowed to vary in order to maintain the original lift coefficient.

After 10 design cycles, the drag coefficient is reduced from 0.0200 to 0.0184. Density contours for the initial and final design are shown in Fig. 17. It is apparent from the increased spacing between the contours that the strength of the shock at the midchord location is somewhat weaker for the final design which accounts for the lower drag.

Summary and Concluding Remarks

Compressible and incompressible versions of an unstructured mesh Navier-Stokes flow solver have been differentiated and the resulting derivatives have been verified by comparisons with finite differences in both two and three dimensions. In this implementation, the turbulence model is fully coupled with the flow equations in order to achieve this consistency. The accuracy of a number of simplifying approximations to the linearizations of the residual have also been examined and none of the approximations yielded derivatives of acceptable accuracy and were often of incorrect sign.

Efficient surface parameterizations have been utilized in both two and three dimensions, and the resulting codes have been integrated with an optimization package. Example optimizations have been demonstrated in both two and three dimensions.

Figure 17. Initial and final density contours for wing.

In order for large scale optimization to become routine, the benefits of parallel architectures should be exploited. Although the three-dimensional flow solver has been parallelized using compiler directives, the parallel efficiency is under 50 percent. Clearly, parallel versions of the codes will have an immediate impact on the ability to design realistic configurations on fine meshes, and this effort is currently underway (see e.g. Ref. 16).

Another area that requires future work is the incorporation of multipoint optimization capability for designing geometries that perform well at off-design conditions. Further development of mesh movement strategies which enable large changes in the geometry are also needed in three dimensions.

Acknowledgments

Appendix A: Governing Equations

Flow Equations

The governing equations are the three-dimensional Reynolds-averaged Navier-Stokes equations. These equations are given as:

$$V\frac{\partial \boldsymbol{Q}}{\partial t} + \oint_\Omega (\vec{\boldsymbol{F}}_i \cdot \hat{n})d\Omega - \oint_\Omega (\vec{\boldsymbol{F}}_v \cdot \hat{n})d\Omega = 0 \qquad (10)$$

where $\hat{n}$ is the outward-pointing normal of the control volume boundary and the vector of conserved variables, $\boldsymbol{Q}$, and inviscid and viscous flux vectors $\vec{\boldsymbol{F}}_i$ and $\vec{\boldsymbol{F}}_v$, are given by

$$\boldsymbol{Q} = \begin{bmatrix} \rho \\ \rho u \\ \rho v \\ \rho w \\ E \end{bmatrix} \qquad (11)$$

$$\vec{\boldsymbol{F}}_i = \begin{bmatrix} \rho u \\ \rho u^2 + p \\ \rho uv \\ \rho uw \\ (E+p)u \end{bmatrix}\hat{i} + \begin{bmatrix} \rho v \\ \rho vu \\ \rho v^2 + p \\ \rho vw \\ (E+p)v \end{bmatrix}\hat{j} + \begin{bmatrix} \rho w \\ \rho wu \\ \rho wv \\ \rho w^2 + p \\ (E+p)w \end{bmatrix}\hat{k} \qquad (12)$$

$$\vec{\boldsymbol{F}}_v = \boldsymbol{f}_v\hat{i} + \boldsymbol{g}_v\hat{j} + \boldsymbol{h}_v\hat{k} \qquad (13)$$

where

$$\boldsymbol{f}_v = \begin{bmatrix} 0 \\ \tau_{xx} \\ \tau_{xy} \\ \tau_{xz} \\ u\tau_{xx} + v\tau_{xy} + w\tau_{xz} - q_x \end{bmatrix} \qquad (14a)$$

$$\boldsymbol{g}_v = \begin{bmatrix} 0 \\ \tau_{yx} \\ \tau_{yy} \\ \tau_{yz} \\ u\tau_{xy} + v\tau_{yy} + w\tau_{zy} - q_y \end{bmatrix} \qquad (14b)$$

$$\boldsymbol{h}_v = \begin{bmatrix} 0 \\ \tau_{zx} \\ \tau_{zy} \\ \tau_{zz} \\ u\tau_{xz} + v\tau_{yz} + w\tau_{zz} - q_z \end{bmatrix} \qquad (14c)$$

The shear stress and heat conduction terms are given by

$$\tau_{xx} = (\mu + \mu_t)\frac{M_\infty}{Re}\frac{2}{3}[2u_x - (v_y + w_z)] \qquad (15)$$

$$\tau_{yy} = (\mu + \mu_t)\frac{M_\infty}{Re}\frac{2}{3}[2v_y - (u_x + w_z)] \qquad (16)$$

$$\tau_{zz} = (\mu + \mu_t)\frac{M_\infty}{Re}\frac{2}{3}[2w_z - (u_x + v_y)] \qquad (17)$$

$$\tau_{xy} = \tau_{yx} = (\mu + \mu_t)\frac{M_\infty}{Re}(u_y + v_x) \qquad (18)$$

$$\tau_{xz} = \tau_{zx} = (\mu + \mu_t)\frac{M_\infty}{Re}(u_z + w_x) \qquad (19)$$

$$\tau_{yz} = \tau_{zy} = (\mu + \mu_t)\frac{M_\infty}{Re}(v_z + w_y) \qquad (20)$$

$$q_x = \frac{-M_\infty}{Re(\gamma - 1)}\left(\frac{\mu}{Pr} + \frac{\mu_t}{Pr_t}\right)\frac{\partial a^2}{\partial x} \qquad (21)$$

$$q_y = \frac{-M_\infty}{Re(\gamma - 1)}\left(\frac{\mu}{Pr} + \frac{\mu_t}{Pr_t}\right)\frac{\partial a^2}{\partial y} \qquad (22)$$

$$q_z = \frac{-M_\infty}{Re(\gamma - 1)}\left(\frac{\mu}{Pr} + \frac{\mu_t}{Pr_t}\right)\frac{\partial a^2}{\partial z} \qquad (23)$$

The equations are closed with the equation of state for a perfect gas

$$p = (\gamma - 1)\left[E - \rho\frac{(u^2 + v^2 + w^2)}{2}\right] \qquad (24)$$

and the laminar viscosity is determined through Sutherland's Law:

$$\mu = \frac{\hat{\mu}}{\hat{\mu}_\infty} = \frac{(1 + C^*)(\hat{T}/\hat{T}_\infty)^{3/2}}{\hat{T}/\hat{T}_\infty + C^*} \qquad (25)$$

where $C^* = 198.6/460.0$ is Sutherland's constant divided by a free-stream reference temperature, which is assumed to be $460°R$.

Turbulence Model

For the current study, the turbulence model of Spalart and Allmaras[27] is used. This is a one-equation turbulence model given as

$$\frac{D\tilde{\upsilon}}{Dt} = \frac{M_\infty}{\sigma Re}\{\nabla \cdot [(\upsilon + (1 + c_{b_2})\tilde{\upsilon})\nabla\tilde{\upsilon}] - c_{b_2}\tilde{\upsilon}\nabla^2\tilde{\upsilon}\} \qquad (26)$$

$$-\frac{M_\infty}{Re}\left(c_{w_1}f_w - \frac{c_{b_1}}{\kappa^2}f_{t_2}\right)\left(\frac{\tilde{\upsilon}}{d}\right)^2 + c_{b_1}(1 - f_{t_2})\tilde{S}\tilde{\upsilon} + \frac{Re}{M_\infty}f_{t_1}\Delta U^2$$

where

$$f_{v_1} = \frac{\chi^3}{\chi^3 + c_{v_1}^3} \qquad (27)$$

$$\chi = \frac{\tilde{\upsilon}}{\upsilon} \qquad (28)$$

$$\tilde{S} = S + \frac{M_\infty}{Re}\frac{\tilde{\upsilon}}{\kappa^2 d^2}f_{v_2} \qquad (29)$$

and

$$f_{v_2} = 1 - \frac{\chi}{1 + \chi f_{v_1}} \qquad (30)$$

In these equations, S is the magnitude of the vorticity, and d is the distance to the nearest wall. The function f_w is given as

$$f_w = g \left(\frac{1 + c_{w_3}^6}{g^6 + c_{w_3}} \right)^{1/6} \qquad (31)$$

where

$$g = r + c_{w_2}(r^6 - r) \qquad (32)$$

and

$$r = \frac{M_\infty}{Re} \frac{\tilde{\upsilon}}{\bar{S} \kappa^2 d^2} \qquad (33)$$

The last term in Eq. 26 is used when specifying the transition location. Because the computations in the present work are all assumed to be fully turbulent, this term is not used. Therefore, definitions of f_{t_1} and f_2, which are associated with these terms, are not given. After Eq. 26 is solved for $\tilde{\upsilon}$, the eddy viscosity is computed as

$$\mu_t = \rho \upsilon_t = \rho \tilde{\upsilon} f_{v_1} \qquad (34)$$

Appendix B: Linearization of Incompressible Solvers

For both two and three dimensions, the incompressible versions of the flow solvers have also been differentiated. The sensitivity derivatives are verified by comparing with derivatives obtained using finite differences.

For the two-dimensional incompressible flow solver, the test case is the 2-element airfoil shown in Fig. 1. The angle of attack is $1°$ and the Reynolds number is 5 million. The design variables are identical to those used for verifying the sensitivity derivatives for the compressible case. Comparisons between computed values and derivatives obtained using finite differences are shown in Tables B1-B4. Derivatives of the lift coefficient with respect to vertical changes in the shape design variables are shown in Table B1 with the corresponding derivatives for drag shown in Table B2. The derivatives obtained for translation of the flap are shown in Tables B3 and B4. As seen in the tables, the derivatives obtained using the adjoint formulation exhibit excellent agreement with the finite differences.

Table B1. Accuracy of two-dimensional incompressible derivatives for lift coefficient (see Fig.1)

	Finite difference	Adjoint	% Diff.
α	0.12050	0.12053	0.025
Point A	-0.97565	-0.97563	-0.002
Point B	0.56795	0.56799	0.007
Point C	-2.0441	-2.0441	0.000
Point D	0.74270	0.74270	0.000

The mesh used for verifying the three-dimensional incompressible linearizations is shown in Fig. 6. The flow conditions are an angle of attack of $3°$ and a Reynolds number of 9 million. The shape design variables are the same as those used in verifying the sensitivity derivatives for the compressible solver. Results are presented in Table B5, and the linearizations are shown to be highly accurate.

Table B2. Accuracy of two-dimensional incompressible derivatives for drag coefficient (see Fig. 1)

	Finite difference	Adjoint	% Diff.
α	0.00807	0.00806	-0.124
Point A	0.22574	0.22574	0.000
Point B	-0.03480	-0.03480	0.000
Point C	0.16820	0.16820	0.000
Point D	0.06251	0.06251	0.000

Table B3. Accuracy of two-dimensional incompressible derivatives of lift coefficient for flap translation

	Finite difference	Adjoint	% Diff.
x-translation	1.3358	1.3361	0.022
y-translation	-6.5537	-6.5537	0.000

Table B4. Accuracy of two-dimensional incompressible derivatives of drag coefficient for flap translation

	Finite difference	Adjoint	% Diff.
x-translation	0.02442	0.02447	0.205
y-translation	-0.22438	-0.22437	-0.004

Table B5. Three-dimensional incompressible derivatives

	Finite difference	Adjoint	% Diff.
α	-0.00307	-0.00307	0.000
Twist #3	0.00922	0.00922	0.000
Shear #3	-0.02648	-0.02648	0.000
Thickness #3	-0.04399	-0.04400	0.023
Camber #4	-1.2594	-1.2594	0.000

References

[1]Anderson, W.K., and Bonhaus, D.L., "An Implicit Upwind Algorithm for Computing Turbulent Flows on Unstructured Grids," *Computers and Fluids*, Vol. 23, No.1, 1994, pp. 1-21.

[2]Anderson, W.K., and Bonhaus, D.L., "Aerodynamic Design on Unstructured Grids for Turbulent Flows," NASA TM 112867, June 1997.

[3]Anderson, W.K., Rausch, R.D., and Bonhaus, D.L., "Implicit/Multigrid Algorithms for Incompressible Turbulent Flows on Unstructured Grids," *J. Comp. Phys.*, Vol. 128, 1996, pp. 391-408.

[4]Anderson, W.K., and Venkatakrishnan, V., "Aerodynamic Design Optimization on Unstructured Grids with a Continuous Adjoint Formulation," AIAA Paper No. 97-0643, 1997.

[5]Bonhaus, D.L., "An Upwind Multigrid Method for Solving Viscous Flows on Unstructured Triangular Meshes," M.S. Thesis, George Washington University, 1993.

[6]Chakravarthy, S.R., and Osher, S., "Numerical Experiments with the Osher Upwind Scheme for the Euler Equations," *AIAA Journal*, Vol. 21, No. 9, 1983, pp. 1241-1248.

[7]Cook, P., McDonald, M., and Firmin, M., "Airfoil RAE 2822—Pressure Distributions and Boundary Layer Wake Measurement.", AGARD AR-138, Paper A6, 1979.

[8]Davidon, W.C., "Variable Metric Method for Minimization," AEC Research and Development Report, ANL-5990, 1959.

[9]Elliott, J., and Peraire, J., "Aerodynamic Design Using Unstructured

Meshes," AIAA Paper No. 96-1941, 1996.

[10]Elliott, J., and Peraire, J., "Aerodynamic Optimization on Unstructured Meshes with Viscous Effects," AIAA Paper No. 97-1849, 1997.

[11]Fletcher, R., and Powell, M.J.D., "A Rapidly Convergent Descent Method for Minimization," *The Computer Journal*, Vol. 6, July 1963, pp. 163-168.

[12]Gopalarathnam, A., Selig, M.S., and Hsu, F., "Design of High-Lift Airfoils for Low-Aspect Ratio Wings with Endplates," AIAA Paper No. 97-2232, 1997.

[13]Hackbusch, W., *Iterative Solution of Large Sparse Systems of Equations*, Springer-Verlag, New York, 1994.

[14]Hou, G. J.-W., Taylor, A.C., and Korivi, V.M., "Discrete Shape Sensitivity Equations for Aerodynamic Problems," *Int. J. for Numerical Methods in Engineering*, Vol. 37, 1994, pp. 2251-2266.

[15]Jameson, A., Pierce, N.A., and Martinelli, L., "Optimum Aerodynamic Design Using the Navier-Stokes Equations," AIAA Paper No. 97-0101, 1997.

[16]Kaushik, D.K., Keyes, D.E., and Smith, B.F., "On the Interaction of Architecture and Algorithm in the Domain-Based Parallelization of an Unstructured Grid Incompressible Flow Code," in Proceedings of the 10th Intl. Conf. on Domain Decomposition Methods, J. Mandel et al., eds., AMS, pp. 311-319.

[17]Marcum, D.L., "Generation of Unstructured Grids for Viscous Flow Applications," AIAA Paper No. 95-0212, 1995.

[18]Mohammadi, B., "Optimal Shape Design, Reverse Mode of Automatic Differentiation and Turbulence." AIAA Paper No. 97-0099, 1997.

[19]Newman, J.C., and Taylor, A.C., "Three-Dimensional Aerodynamic Shape Sensitivity Analysis and Design Optimization Using the Euler Equations on Unstructured Grids," AIAA Paper No. 96-2464, 1996.

[20]Pirzadeh, S., "Viscous Unstructured Three-Dimensional Grids by the Advancing-Layers Method," AIAA 94-0417, 1994.

[21]Roe, P.L., "Approximate Riemann Solvers, Parameter Vectors, and Difference Schemes," *J. Comp. Phys.*, Vol. 43, No. 2, 1981, pp. 357-372.

[22]Saad, Y., and Schultz, M.H., "GMRES: A Generalized Minimal Residual Algorithm for Solving Nonsymmetric Linear Systems," *SIAM J. Sci. Stat. Comput.*, Vol. 7, 1986, pp. 856-869.

[23]Samareh, J., "Geometry Modeling and Grid Generation for Design and Optimization," ICASE/LaRC/NSF/ARO Workshop on Computational Aerosciences in the 21st Century," April 22-24, 1998.

[24]Schmitt, V., and Charpin, F., "Pressure Distributions on the ONERA-M6 Wing at Transonic Mach Numbers," Experimental Data Base for Computer Program Assessment, AGARD-AR-138, May 1979, pp. B1-1-B1-44.

[25]Sherman, L.L., Taylor, A.C., Green, L.L., Newman, P.A., Hou, G.J.-W., and Korivi, V.M., "First- and Second-Order Aerodynamic Sensitivity Derivatives via Automatic Differentiation with Incremental Iterative Methods," AIAA Paper No. 94-4262, 1994.

[26]Soemarwoto, B., "Multipoint Aerodynamic Design by Optimization," Ph.D. Thesis, Delft University of Technology, 1996.

[27]Spalart, P.R., and Allmaras, S.R., "A One-Equation Turbulence Model for Aerodynamic Flows," AIAA Paper No. 92-0439, 1991.

[28]Suddhoo, A., and Hall, I.M., "Test Cases for the Plane Potential Flow Past Multi-Element Airfoils," *Aeronautical Journal*, December 1985.

[29]Van Leer, B., "Flux Vector Splitting for the Euler Equations," Lecture Notes in Physics, Vol. 170, 1982, pp. 501-512.

[30]Venkatakrishnan, V., and Mavriplis, D.J., "Implicit Method for the Computation of Unsteady Flows on Unstructured Grids," *J. Comp. Phys.*, Vol. 127, 1996, pp. 380-397.

[31]Williams, B.R., "An Exact Test Case for the Plane Potential Flow About Two Adjacent Lifting Aerofoils," R. & M. No. 3717, British Aeronautical Research Counci, 1973.

[32]Wrenn, G.A., "An Indirect Method for Numerical Optimization Using the Kresselmeier-Steinhauser Function," NASA CR 4220, March 1989.